

Article

# Modeling and Analysis of Sea-Surface Vehicle System for Underwater Mapping Using Single-Beam Echosounder

Seda Karadeniz Kartal <sup>1,\*</sup>, Rifat Hacıoğlu <sup>1</sup>, K. Sedar Görmüş <sup>2</sup>, Ş. Hakan Kutoğlu <sup>2</sup>  
and M. Kemal Leblebicioğlu <sup>3</sup>

<sup>1</sup> Electrical and Electronic Engineering Department, Zonguldak Bulent Ecevit University, 67100 Zonguldak, Turkey

<sup>2</sup> Geomatic Engineering Department, Zonguldak Bulent Ecevit University, 67100 Zonguldak, Turkey

<sup>3</sup> Electrical and Electronic Engineering Department, Middle East Technical University, 06800 Ankara, Turkey

\* Correspondence: sedakaradeniz@gmail.com

**Abstract:** Detailed knowledge on the shape of the seafloor is crucial for many researchers. Bathymetric data are critical for navigational safety and are used for underwater mapping. This study develops a sea-surface vehicle (SSV) system for underwater mapping by using both bathymetric data from a low-cost single-beam echosounder located on the SSV, and the navigation data of the SSV. The navigation of the SSV was obtained using a global positioning system (GPS). The effect of changing bathymetric and navigation data due to external disturbances such as wind and waves on the map was analyzed. The sea-bottom slope angles, which are effective in changing bathymetric data, were estimated and corrected in relation to the estimated angles in a particular mapped area for more accurate underwater mapping. Additionally, the effects of the grid range of the mapped area, beam angle of the echosounder, and position of the echosounder on the underwater mapping were analyzed. These analyses were based on simulation data, and were performed in a MATLAB, HYPACK, and Global Mapper environment. An underwater map was also obtained in the Kozlu/Zonguldak area, Black Sea by using a single-beam echosounder located on the SSV. This map was improved by estimating sea-bottom slope angles and the corrected bathymetric data to obtain a more accurate underwater map of the area. The experimental and simulation results were compared, focusing on the sea-bottom slope changes, sea-surface disturbances, bathymetry grid range changes, and draft effects.

**Keywords:** single-beam echosounder; underwater mapping; bathymetry; seafloor slope angle; echosounder beam angle; sea-surface vehicle; grid range



**Citation:** Kartal, S.K.; Hacıoğlu, R.; Görmüş, K.S.; Kutoğlu, Ş.H.; Leblebicioğlu, M.K. Modeling and Analysis of Sea-Surface Vehicle System for Underwater Mapping Using Single-Beam Echosounder. *J. Mar. Sci. Eng.* **2022**, *10*, 1349. <https://doi.org/10.3390/jmse10101349>

Academic Editor: Weicheng Cui

Received: 8 August 2022

Accepted: 14 September 2022

Published: 22 September 2022

**Publisher's Note:** MDPI stays neutral with regard to jurisdictional claims in published maps and institutional affiliations.



**Copyright:** © 2022 by the authors. Licensee MDPI, Basel, Switzerland. This article is an open access article distributed under the terms and conditions of the Creative Commons Attribution (CC BY) license (<https://creativecommons.org/licenses/by/4.0/>).

## 1. Introduction

Underwater topography is important for the design and application of water structures such as pipelines, seaports, and breakwaters in seas and lakes [1–3]. The study of underwater topography is bathymetry, and the measurement process is called hydrographic surveying. Underwater mapping techniques are commonly named according to the equipment used for measurements, such as lath, rope, and wire sounders. These techniques have been used to measure the depth from the seafloor for underwater mapping, referred to as bathymetric data. The current technology uses acoustic sounders. Although bathymetric measurements using multibeam echosounders are faster and more sensitive for underwater mapping, single-beam echosounders are cheaper [4,5]. Therefore, practitioners commonly prefer to apply the single-beam technique [6]. In this study, we investigate the underwater mapping problem using bathymetric data measured using a single-beam echosounder; both simulation and experimental data were obtained.

Error sources in hydrographic surveying detected through echosounders are based on electrical and acoustical factors, such as sound velocity variation and signal travel time (clock) errors, and the change effects of the sea surface and seafloor [7,8].

The important effect of bathymetric measurements using a single-beam echosounder is the seafloor slope angle [9]. In previous studies, many methods were used to describe the seafloor. Backscatter characteristics are commonly used in seafloor characterization. The most significant uncertainty in backscatter data is the effect of the seafloor slope. A standard method of seafloor slope estimation and correction was proposed to achieve repeatable and accurate backscatter results [10]. The correlation backscatter characteristics and the seafloor-insonification area changes with beam width, incidence angle, water depth, and sonar pulse length were obtained [11]. The seafloor was classified according to frequency shifts that occurred when a high-frequency pulse backscattered from the seafloor [12], and the measured depth was corrected with the frequency shifts. In another study, the seafloor was classified according to echo durations, such as short, long, and extended echoes [13]. An algorithm was presented for the automatic compensation of seismic amplitudes for the seafloor slope and depth [14]. In the inclined seafloor, accurate measurements of the depth were achieved by turning the echosounder head on the basis of the value of the angle of inclination [15]. The challenges associated with evaluating the bottom-angle estimation performance for using a multibeam echosounder were detailed in a prior work [16]. Bathymetric data were measured by integrating the echosounder on both surface and underwater vehicles [17]. The seafloor slope angle distribution of the bathymetry-measuring echosounder integrated with an autonomous underwater vehicle was established. The slope angle was calculated, and the seafloor displacement error was estimated [18]. However, in all these studies, the angle of the seafloor slope was considered in one axis. In contrast to the two-dimensional state of the seafloor in previous studies [19], the slope angles for the three-dimensional seafloor are defined in (5) and (6).

Because a single-beam echosounder measures the closest distance between the seafloor and sea-surface vehicle, bathymetric data measured using an echosounder should be corrected when the seafloor is inclined. Actual bathymetric data are the depth at which the sonar is perpendicular to the sea bottom [7]. In the case of an inclined sea bottom, the chosen grid range is effective for bathymetric measurements [20,21]. The effect of the grid range on measured bathymetry was analyzed with a digital terrain model for the sloping seafloor. This shows that the grid range can be selected on the basis of local point density, as was the aim of the investigation in [22]. The grid range's impact in interpolating sparse bathymetric data was established through a direct Monte Carlo simulation [23]. The grid range value should be selected without missed points in the mapped area, as in (8), and bathymetric measurements should be performed by dividing the mapped area into equal grid ranges. In the case of the bathymetric data obtained using a single-beam sonar, a narrow or wide beam angle affects the accuracy of the underwater map [24,25]. The beam angle depends on the transducer size of the sonar and the wavelength. The higher the frequency and the larger the transducer are, the narrower the beam angle is [26,27]. The measured depth value may change because of the oscillation of the vehicle in which the sonar is integrated with the external disturbance effect, and the positions in the x and y axes based on the measured depth should be corrected according to this oscillation value [28,29].

In this study, the effects of the sea-bottom slope, grid range, beam angle, external disturbances, and value of the transducer (draft of echosounder) were analyzed on the basis of bathymetric data of an underwater map in a three-dimensional (3D) inclined sea bottom. The main contributions of this study are as follows:

- In previous studies, bathymetric data measured using a single-beam sonar were analyzed for cases in which the seafloor was inclined in only one axis. In contrast, two axes' seafloor slope angles are proposed and discussed here for a 3D seafloor.
- The measured bathymetric data are corrected when the seafloor angles are inclined in two axes after the seafloor angles are estimated using the proposed approach.
- To avoid missing the bathymetric measurement of any point in the mapped area, we successfully selected a grid range value on the basis of its geometry.

- The effects of the sonar beam angle, external disturbance, draft of the sonar on the measured bathymetric data and the underwater map, the seafloor slope, and grid range were analyzed in detail.

The remainder of this paper is organized as follows. Section 2 presents the single-beam echosounder model. We provide a detailed definition of the effects of the underwater map's accuracy in Section 3. Section 4 presents an underwater mapping simulator. Section 5 details the underwater mapping experiments. Lastly, the conclusion and future work are presented in Section 6.

## 2. Single-Beam Echosounder Model

A sound navigation and ranging (sonar) device, that is, the echosounder, uses an acoustic signal to measure the depth from the sea floor [30]. Depth measurement is affected by the electrical and acoustic parameters of the sonar device. Acoustic parameters such as frequency, bandwidth, and signal length determine the propagation characteristics of underwater acoustic signals. The sonar equation can be used to understand and analyze the sonar performance. This equation is composed of the electrical parameters of the sonar, and it defines the signal or sound detection as echo excess (EE):  $EE = SL - 2TL - (NL - DI) + BS - DT$  [31], where SL is the source level, TL is the transmission loss, NL is the noise level, DI is the directivity index, BS is the bottom backscattering strength, and DT is the detection threshold.

In this study, a single-beam echosounder was used to measure the depth from the seafloor. This echosounder was integrated into a sea-surface vehicle. After the acoustic signal had been sent from a single-beam echosounder, it reached the sea floor, and the first returning signal was received from the echosounder [7]. Figure 1 shows the beam coverage of the seafloor as conical for a single-beam echosounder at the given grid range ( $g_r$ ). The beam coverage of the seafloor  $a$  and depth  $h_m$  are calculated in (1).

$$a = 2h_m \tan \frac{\varphi}{2}, h_m = \frac{1}{2} \Delta t \cdot c \quad (1)$$

where  $a$  is the diameter of the area covered by the echo,  $h_m$  is the depth value,  $\varphi$ , is the beam angle,  $\Delta t$  is the time interval between sending and receiving the transmitted signal, and  $c$  is the acoustic signal.

The single-beam echosounder measures the distance between the vehicle on which the single-beam sonar is located and the seafloor level [31]. This distance value is also obtained in relation to the position of the vehicle as follows.

$$h_m = \sqrt{(x - x_s)^2 + (y - y_s)^2 + (z - z_s)^2} \quad (2)$$

where  $h_m$  denotes the measured bathymetric data,  $x_s, y_s, z_s$  denote the position of the single-beam echosounder, and  $x, y, z$  denote the position of mapped area.

For high accuracy and a clear record of the bathymetric data, electrical and acoustic sonar parameters must be set correctly before measurement. The most important parameters are power, gain, recording density, pulse length, scale, phase scale, draft, and sound velocity. Other important parameters that affect the accuracy of bathymetric data are the navigation data of the vehicle on which the sonar is located, the beam angle of the sonar, the grid range in the mapped area, and the sea-bottom slope angle [32–34].

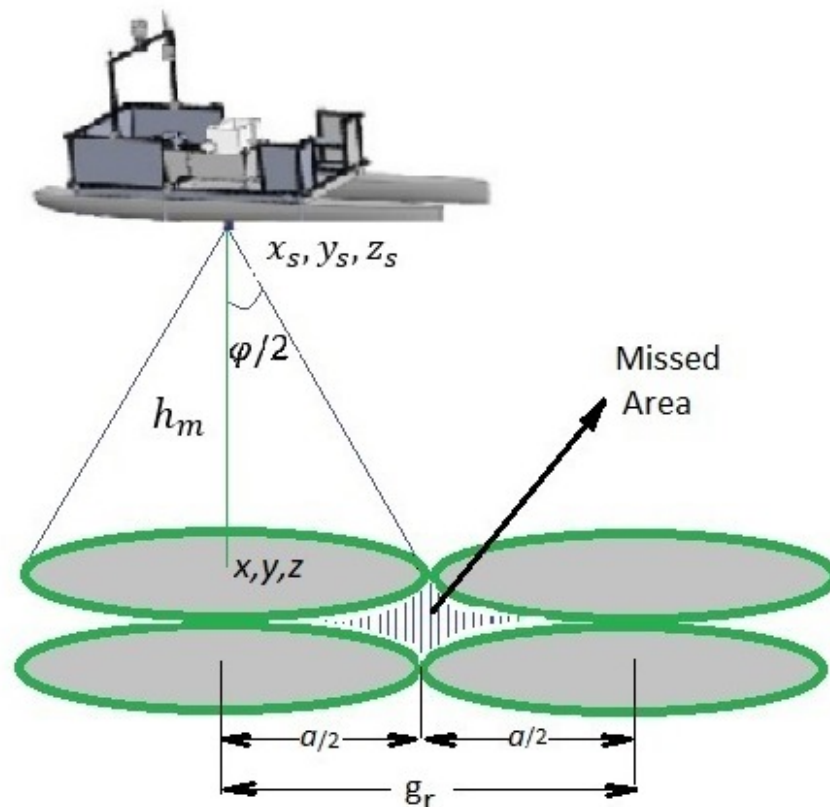


Figure 1. Seafloor coverage in the single-beam echosounder for a given grid range ( $g_r$ ).

### 3. Definition of the Effects of Underwater Map Accuracy

In this section, the effects of the seafloor slope, grid range, beam angle of the echosounder, echosounder position, and external distribution on the accuracy of the underwater map are defined.

#### 3.1. Seafloor Slope Effect

The sea-bottom slope angle is an important factor to consider when measuring bathymetry with a single-beam echosounder. Because a single-beam echosounder measures the closest distance between the seafloor and sea-surface vehicle, bathymetric data measured using an echosounder should be corrected when the seafloor is curved.

The acoustic wave is transmitted conically from a single-beam echosounder. This acoustic wave is first reflected from the seafloor and returned to the echosounder; the depth was calculated as shown in (1). The measured depth was equal to the actual depth of a flat seafloor, as shown in Figure 2a. However, the seafloor is not always flat, as shown in Figure 2b,c. Thus, the measured depth is related to the seafloor slope angles. Figure 2 shows the relationship between the actual and measured depths with respect to seafloor slope angles for the 3D sea-bottom area. In Figure 2,  $h_m$  is the measured depth, and  $h$  is the actual depth.

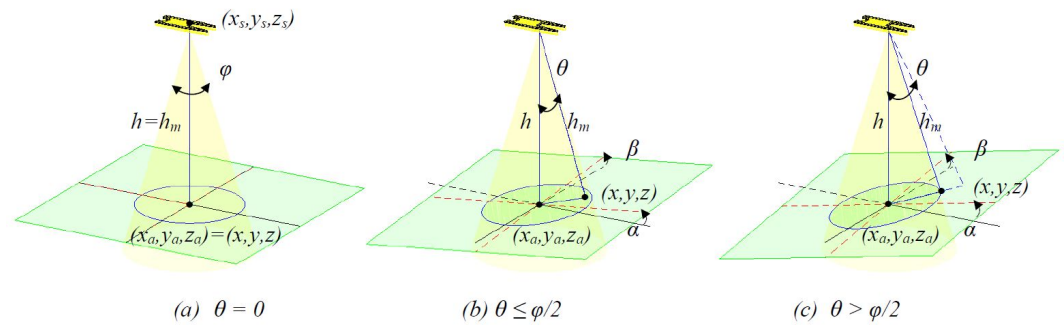


**Figure 2.** (a) Sea-bottom coverage for a flat sea floor. In this situation,  $h_m = h$ . (b) Theta angle ( $\theta$ ) related to the sea floor slope is inside the insonified (conical) area for inclined sea floor. In this situation,  $h_m \neq h$ . (c) Theta angle related to the sea floor slope is outside the insonified (conical) area for an inclined sea floor. In this situation,  $h_m \neq h$ .

**Definition 1.** Given the beam angle of the single-beam echosounder ( $\varphi$ ), the relationship between actual depth  $h_a(k)$  and measured depth (bathymetric data)  $h_m(k)$  with respect to sea-bottom angles  $\alpha(k)$  in the  $x$  axis and  $\beta(k)$  in the  $y$  axis at the  $k$ th position of  $x(k)$ ,  $y(k)$  is defined as

$$\cos \theta(k) = \cos \alpha(k) \cos \beta(k) \tag{3}$$

so that

$$h_m(k) = h_a(k) \begin{cases} \cos \theta(k), & 0 \leq |\theta(k)| \leq \frac{\varphi}{2} \\ \frac{\cos \theta(k)}{\cos(\theta(k) - \frac{\varphi}{2})}, & |\theta(k)| \geq \frac{\varphi}{2} \end{cases} \tag{4}$$

Hence, at the  $k$ th position,  $(x(k), y(k))$ ,  $h_a(k)$  can be calculated using (4).

**Definition 2.** The sea-bottom slope angles along the  $x$  and  $y$  axes are estimated using the measured depth values at the sampling interval,  $g_m$ , and the beam angle of the echosounder as follows.

$$\tan \hat{\alpha}(k) = \frac{h_m(x(k), y(k)) - h_m(x(k-1), y(k))}{g_m} \tag{5}$$

$k = 2, \dots, K$

$$\tan \hat{\beta}(k) = \frac{h_m(x(k), y(k)) - h_m(x(k), y(k-1))}{g_m} \tag{6}$$

$k = 2, \dots, K$

where  $\hat{\alpha}(1) = 0$ ,  $\hat{\beta}(1) = 0$ , and  $K$  are the total sampling data in the mapped area. After the sea-bottom slope angles had been estimated, the measured depth values (bathymetric data) were corrected for the two conditions using (4). By defining  $g_m$ , sampling interval (distance), and  $g_r$ , the grid range in the mapped area,  $h_m(k)$ , is the  $k$ -th measured value obtained through linear interpolation using the measured depth value at sampling distance  $g_m$  in each grid range represented by  $g_r$ . For  $g_m = 0.2$  m, five sampling points between two measurements were obtained at  $g_r = 1$  m; for  $g_m = 0.2$  m, 25 sampling points were obtained between each consecutive measurement at  $g_r = 5$  m. One can use neighborhood measured values to estimate  $\alpha$  and  $\beta$  as in [35,36] instead of (5) and (6).

**Lemma 1.** Actual depth  $h_a(k)$  can be obtained using (4) with a known position  $(x(k), y(k))$ , and beam angle  $\varphi$  using measured depth  $h_m(k)$ . Furthermore, estimated depth value  $\hat{h}_a(k)$  converges to the value of the actual depth if the sea-bottom slope angle estimates (5) and (6) approach  $\alpha(k)$  and  $\beta(k)$ .

**Proof.** It is straightforward to prove that, if in Definition 2, the sea-bottom angle estimates both  $\alpha$  and  $\beta$  with an appropriate gm sampling distance, then

$$\hat{h}_a(k) = h_m(k) \begin{cases} \frac{1}{\cos\hat{\theta}(k)}, & 0 \leq |\hat{\theta}(k)| \leq \frac{\varphi}{2} \\ \frac{\cos(\hat{\theta}(k) - \frac{\varphi}{2})}{\cos\hat{\theta}(k)}, & |\hat{\theta}(k)| > \frac{\varphi}{2} \end{cases} \quad (7)$$

where the angle is  $\cos\hat{\theta}(k) = \cos\hat{\alpha}(k)\cos\hat{\beta}(k)$ .  $\square$

### 3.2. Grid Range Effect

The selection of the grid range of the mapped region affects the accuracy of the underwater topography. Generally, more measurement data are obtained from the mapped area by choosing a low grid range. Thus, a high-resolution map was obtained. In areas where the seafloor is sloping, grid spacing selection is more effective. If the grid range value is chosen to be larger than the sea-bottom coverage area on the basis of beam angle and depth, measurements of some points can be missed.

**Lemma 2.** *Choosing smaller grid spacing than the coverage area,  $g_r < 2z_m \tan \frac{\varphi}{2}$  was still not sufficient to map the entire area, as shown in Figure 1. To map all points without missing any in the mapped area, grid spacing corresponding to overlapping circles should be chosen. Hence, the grid range value was selected from the geometry shown in Figure 1:*

$$g_r \leq \sqrt{2}z_m \tan \frac{\varphi}{2} \quad (8)$$

where  $g_r$  is the selection of the grid range value for the mapped area,  $a$  is the diameter of the covered area, and  $\varphi$  is the beam angle of the single-beam echosounder.

The seafloor slope angles depend on the value of the measured depth in each grid interval interpolated at a certain interval ( $g_m$ ), as shown in (5) and (6). The estimated seafloor angles are different for grid values of 5 m and 1 m. By choosing a small grid range value in the inclined sea-bottom area, the estimated seafloor angles are closer to the actual angle values.

### 3.3. Beam Angle of Echosounder Effect

For bathymetric data obtained using a single-beam sonar, a narrow or wide beam angle affects the accuracy of the underwater map. The beam angle depends on the transducer size of the sonar and the wavelength. The higher the frequency and the larger the transducer are, the narrower the beam angle is. Although we obtained a high-resolution underwater map when using the narrow-angle sonar, the measurement of some points may have been missed owing to external disturbance effects, such as waves and the wind, especially on a sloping seafloor. The optimal beam angle should be chosen according to the presence of the seafloor and external disturbances. The definition of the beam angle effect is given in (4) for two conditions when the sea floor is inclined.

### 3.4. External Disturbance Effect

The rotations of the sea-surface vehicle about the  $x$ ,  $y$ , and  $z$  axes are defined as roll, pitch, and yaw, respectively, and are measured using an inertial measurement system (INS) [37,38]. The sea-surface vehicle’s attitudes such as roll and pitch are zero without disturbances, and the echosounder is perpendicular to the seafloor. Changing the sea-surface vehicle motion with external disturbances, such as wind and waves, affects the measured bathymetric data and position of the sea-surface vehicle in which the sonar is integrated.

The sea-surface vehicle oscillates when external disturbances affect the attitudes of the vehicle, which are different from those of the starting level. If the angle of these oscillations (roll and pitch) is greater than half the beam angle, the sea-bottom coverage area is changed. The external disturbance effects, in degrees, in the  $x$  and  $y$  axes are defined as  $\delta_x$  and  $\delta_y$  to

the oscillation of the sea-surface vehicle, as shown in Figure 3c. Rotating the yaw angle along the z axis does not affect the measured bathymetric data [39].

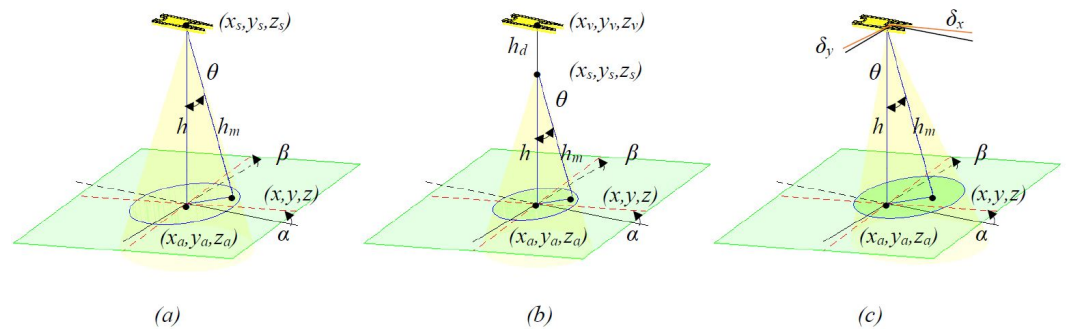


**Figure 3.** (a) Depth measurement without external disturbances and draft of echosounder at the inclined seafloor. (b) Depth measurement with a draft of the echosounder at inclined seafloor. In this situation, the echosounder is below the sea surface by an amount of  $h_d$ . (c) Depth measurement with external disturbances in the x and y axes ( $\delta_x$  and  $\delta_y$ ) at the inclined seafloor.

**Definition 3.** The positions of the sea-surface vehicle in the x and y axes are corrected in relation to the roll, pitch, and yaw angles owing to oscillations using the rotation matrix for measured bathymetric data [29,40]. If the vehicle rotates around the z, y, and x axes with  $\sigma$ ,  $\gamma$ , and  $\phi$ , respectively, with an external distribution effect, then the position of the sea-surface vehicle based on the measured depth is corrected using rotation transformation matrix C as follows:

$$\eta' = \begin{bmatrix} c\sigma c\gamma & -s\sigma c\phi + c\sigma s\gamma s\phi & s\sigma s\phi + c\sigma c\phi s\gamma \\ s\sigma c\gamma & c\sigma c\phi + s\phi s\gamma s\sigma & -c\sigma s\phi + s\gamma s\sigma c\phi \\ -s\gamma & c\gamma s\phi & c\gamma c\phi \end{bmatrix} \eta \tag{9}$$

where  $\eta' = [x_s', y_s', z_s']^T$  is the corrected position vector of the surface vehicle, and  $\eta = [x_s, y_s, z_s]^T$  is the measured position vector of the surface vehicle.

It is assumed that, in the case of small angle changes, ( $\cos(\cdot) = 1, \sin(\cdot) = 0$ ) transformation matrices are identity matrices, and position changes are neglected where  $c. = \cos(\cdot)$  and  $s. = \sin(\cdot)$ .

### 3.5. Echosounder Position Effect

The distance between the place where the sonar transducer is mounted on the surface vehicle and the water surface, called the draft, affects the accuracy of underwater mapping. Draft value  $h_d$ , shown in Figure 3b, should be added to the measured depth value from the single-beam echosounder.

**Definition 4.** As the sonar moves away from the sea surface and approaches the seafloor, higher resolution measurements are obtained. Measurements closer to the seafloor are obtained by integrating the sonar into an underwater vehicle. When the beam angle is constant, as the sonar approaches the sea floor, the coverage of the single-beam sonar narrows, as indicated in (1), resulting in a higher resolution underwater map. The difference in distance between the sea level and the transducer of the echosounder is defined as draft (or bias). The distance between the acoustic sonar and the measurement station (sea-surface vehicle used in this study) is represented by  $h_d$ , as shown in Figure 3b. This draft value must be added to each measured depth value.

## 4. Underwater Mapping Simulator

The simulator block diagram for underwater mapping is shown in Figure 4. First, the single-beam echosounder parameters and environmental parameters were set, and the background sea-floor map was generated. The sonar model was used to generate the distance between the vehicle on which the sonar was located and the seafloor. The sea-bottom slope angles were estimated using the measured depth values, as in Definition 2. Then,

the measured depth was corrected on the basis of the estimated sea-bottom slope angles. The corrected depth value and navigation data of the sea-surface vehicle were integrated to compose the underwater map. The underwater map simulator block shows that the sea surface, sea-bottom effects, and the grid range and beam angle play an important role in improving the accuracy of an underwater map.

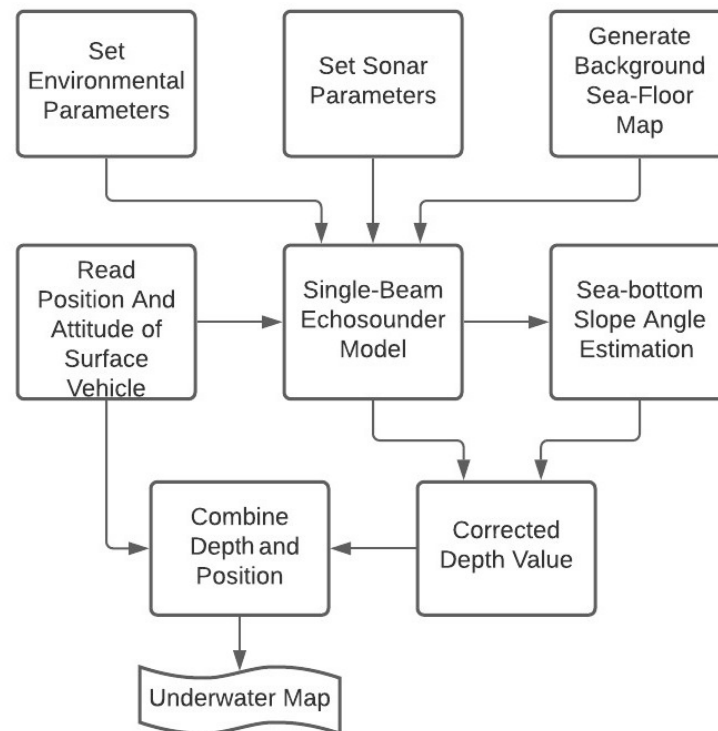


**Figure 4.** Block diagram of the underwater mapping simulator.

Underwater mapping is performed according to

- the seafloor slope angle;
- the beam angle of the echosounder;
- the grid range in the mapped area;
- the position of the sonar's transducer;
- the external disturbances to the motion of the sea-surface vehicle in order to show the single-beam echosounder performance.

#### 4.1. Topographical Settings

The underwater map was generated using a single-beam echosounder for real-time measurements. First, underwater topography based on simulation data was generated, as shown in Figure 5. Subsequently, the bathymetric data (distance between the sea-surface vehicle on which a single-beam echosounder was mounted and the sea-bottom) and sea-bottom angles were estimated from the measured depth related to each  $k$ -th position in the  $x$  and  $y$  axes. Thus, the bathymetric data were corrected, and the corrected underwater map was obtained. The analysis of underwater mapping based on simulation data was performed in a MATLAB environment.

Figure 5 shows the generated seafloor area. The depth variation is provided in  $100 \times 80$  m in the  $x$  and  $y$  axes with a sampling range of 0.2 m. Here, actual depth  $h_a$  values are between 10 and 55 m, and sea-bottom angles are between  $-50^\circ$  and  $50^\circ$  for  $\alpha$ , and  $-40^\circ$  and  $40^\circ$  for  $\beta$ .

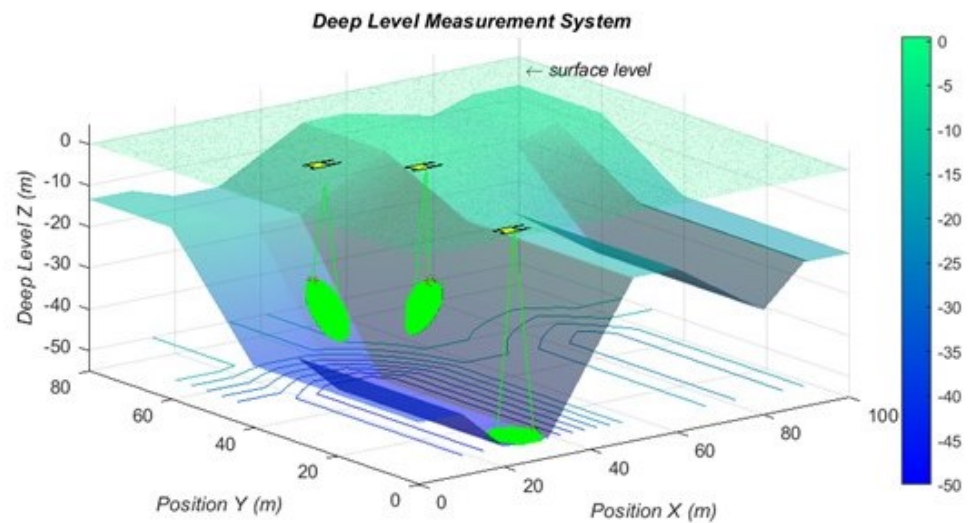


**Figure 5.** Generated underwater topography based on simulation.

To compare all these effects, given that  $K_1$  and  $K_2$  are the total sampling data for the grid range in the  $x$  and  $y$  axes for  $k_1 = 1, \dots, K_1$  and  $k_2 = 1, \dots, K_2$ , we used the measured error:

$$E_m(k_1, k_2) = h_a(x(k_1), y(k_2)) - h_m(x(k_1), y(k_2)) \tag{10}$$

and estimated error

$$E_e(k_1, k_2) = h_a(x(k_1), y(k_2)) - \hat{h}_a(x(k_1), y(k_2)) \tag{11}$$

where  $h_a$  is the actual depth,  $h_m$  is the measured depth, and  $\hat{h}_a$  is the estimated depth using (7) at  $k_1$ th and  $k_2$ th position in the  $x$  and  $y$  axes, respectively. Total measured and estimated absolute errors were calculated with the sum of the measured and estimated absolute errors using (10) and (11). Further, root mean square (RMS) measurements and estimated error calculations are performed using the sum of the squares of the measurements and the estimated error divided by the total sampling data.

#### 4.2. Analysis of Underwater Mapping Accuracy

##### 4.2.1. Analysis of the Sea-Bottom Slope Effect

Measured bathymetric data are calculated as the closest distance between the sea-surface vehicle, assuming that the vehicle is at the water level, and the seafloor, as shown in (2). The deep level measurement occurs with these generated bathymetric data, as depicted in the upper side of Figure 6. Figure 6 shows the estimated sea-bottom slope angles in the  $x$  axis, called  $\alpha$ , and in the  $y$  axis, called  $\beta$ , using the generated sea-bottom data at each  $k$ -th position, which is calculated using (5) and (6) of Definition 2. Bathymetric data measurements were performed with a single-beam sonar for a 10 m grid range and the  $10^\circ$  beam angle of the echosounder without external disturbances. Figure 6 shows that there were cases in which the estimated sea-bottom angles were both smaller and larger than half of the beam angle.

Figure 6 shows the underwater map with the bathymetric value of the area corrected according to the estimated bottom slope angles based on Lemma 1. The topography based on the corrected bathymetric data was more inclined compared with the measured bathymetric data.

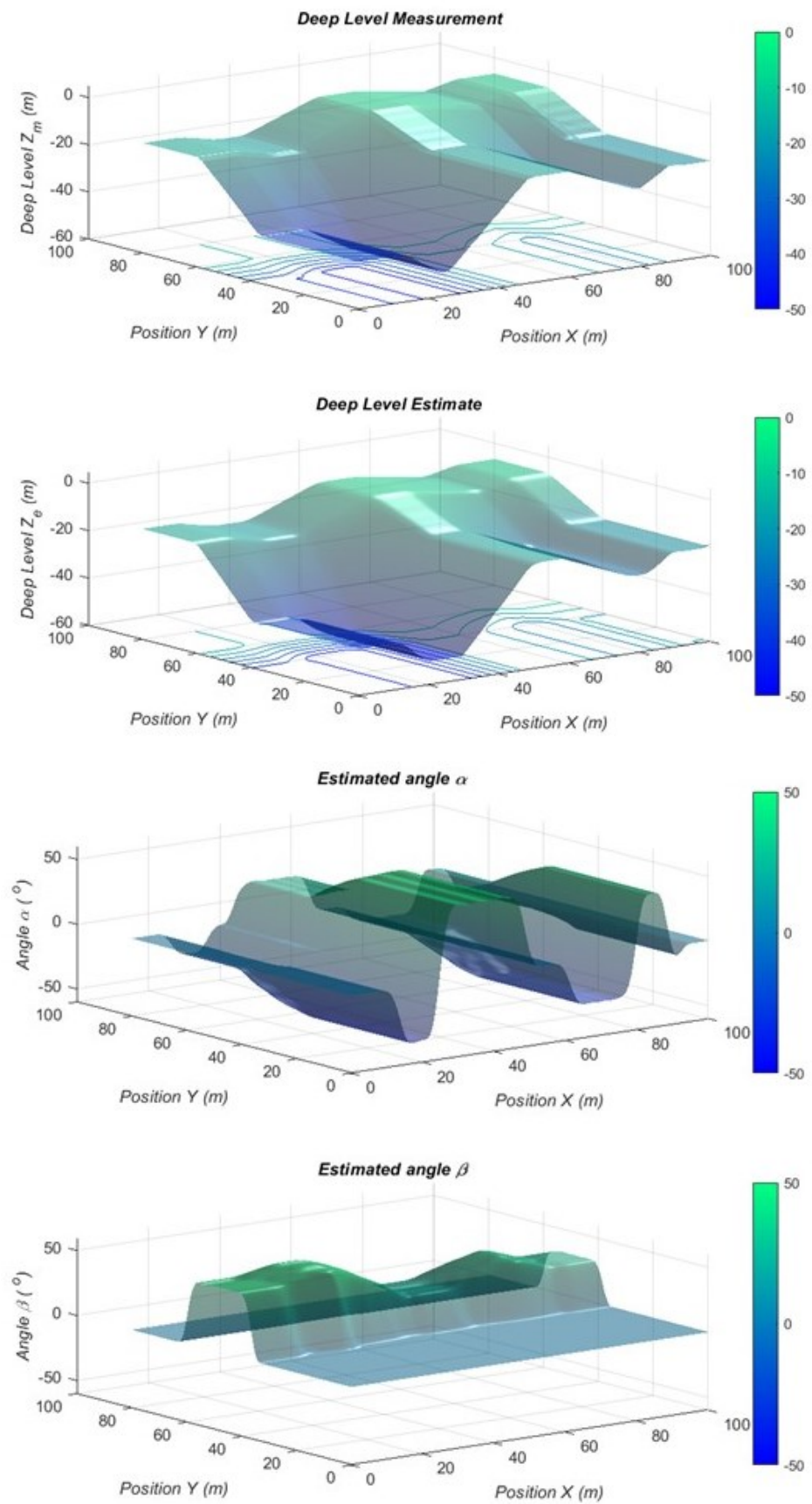


**Figure 6.** Underwater map with measured depth level and underwater map with estimated depth level. Estimated sea-bottom slope angles in the  $x$  ( $\alpha$ ) and  $y$  ( $\beta$ ) axes.

Errors related to the measured and estimated depths were analyzed to determine the accuracy of the underwater map. The total absolute error between the actual and measured depths was calculated using  $E_m$  in (10); the measured error for a particular area is shown in the upper part of Figure 7. The estimated error was calculated using  $E_e$  in (11) using the difference between the actual and estimated depths, and the estimated error for a particular area is shown on the bottom side of Figure 7; the measured error increased with the sea-bottom slope effect, while the estimated error varied around zero.

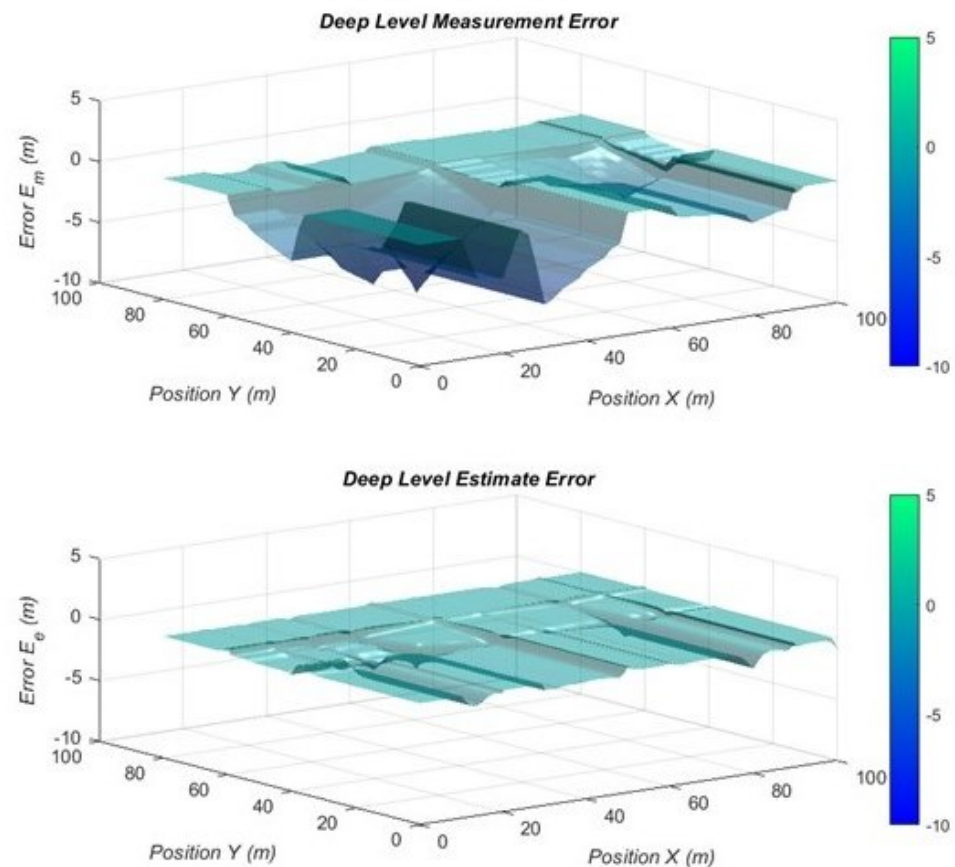
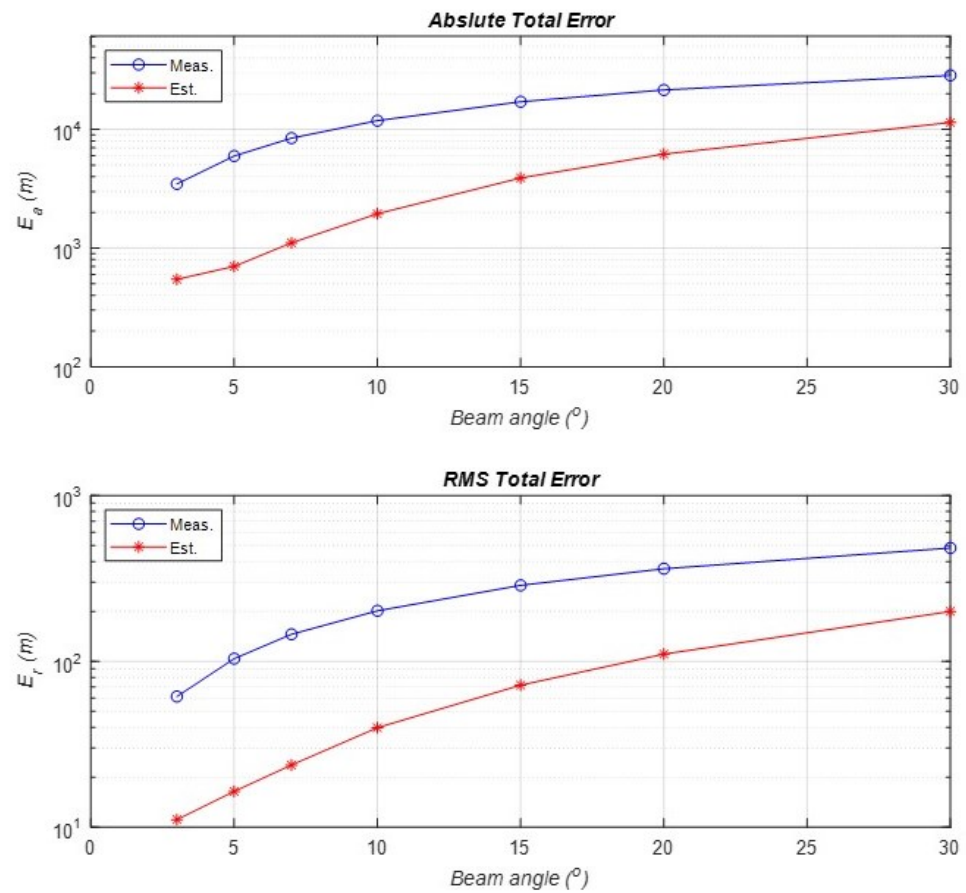


Figure 7. (top) Measured and (bottom) estimated error for a particular area.

#### 4.2.2. Analysis of the Grid Range and Beam Angle Effect

The grid range and beam angle effects that affect the accuracy of the bathymetry measurements were analyzed. The total absolute and root mean square measured errors (blue line), and the total absolute and RMS estimated errors (red line) at different beam angles based on the constant grid range (1 m) without external disturbances are shown in Figure 8. It was assumed that the depth of the vehicle from the sea surface was zero under this condition. The total absolute measured error was  $12 \times 10^3$  m, the total absolute estimated error was  $2 \times 10^3$  m, the total RMS measured error is 200 m, and the total RMS estimated error was 40 m at  $\varphi = 10^\circ$ ,  $g_r = 1$  m,  $\delta_x = 0$ ,  $\delta_y = 0$ , and  $h_d = 0$ . When the beam angle increased to  $30^\circ$ , the total absolute measured error became  $3 \times 10^4$  m. When the total absolute estimated error was  $1.2 \times 10^4$  m, the total RMS measured error was  $5 \times 10^2$  m, and the total RMS estimated error was  $2 \times 10^2$  m at  $g_r = 1$  m,  $\delta_x = 0$ ,  $\delta_y = 0$ , and  $h_d = 0$ .

Results show that the absolute measured and estimated errors increased when the beam angle of the single-beam echosounder increased. In addition, the estimated error was smaller than the measured error when the beam angle was increased. The measured and estimated errors improved with a narrow beam angle in the absence of external disturbances.



**Figure 8.** Variation in the absolute and RMS total measured errors (blue lines), and the absolute and RMS total estimated errors (red lines) for different beam angles at a constant grid range without external disturbances.

Figure 9 shows the absolute total and RMS measured errors (blue line), and the absolute total and RMS estimated errors (red line) at different grid values according to a constant beam angle, (15°) without external disturbances. It was assumed that the depth of the vehicle from the sea-surface was zero in this condition. The total absolute measured error was  $12 \times 10^3$  m, total absolute estimated error was  $2 \times 10^3$  m, total RMS measured error was 200 m, and total RMS estimated error was 40 m at the  $g_r = 2$  m,  $\varphi = 15^\circ$ ,  $\delta_x = 0$ ,  $\delta_y = 0$ , and  $h_d = 0$ . When the grid range increased to 20 m, the total absolute measured error became  $2 \times 10^4$  m, total absolute estimated error was  $1.8 \times 10^4$  m, RMS measured error was  $3 \times 10^2$  m, and RMS estimated error was  $2.5 \times 10^2$  m at  $\varphi = 15^\circ$ ,  $\delta_x = 0$ ,  $\delta_y = 0$ , and  $h_d = 0$ .

Simulation results show that the absolute measured and estimated errors increased if the grid range increased. In addition, the estimated error was smaller than the absolute error when the grid range increased. The measured and estimated errors improved with a low grid range in the absence of external disturbances.

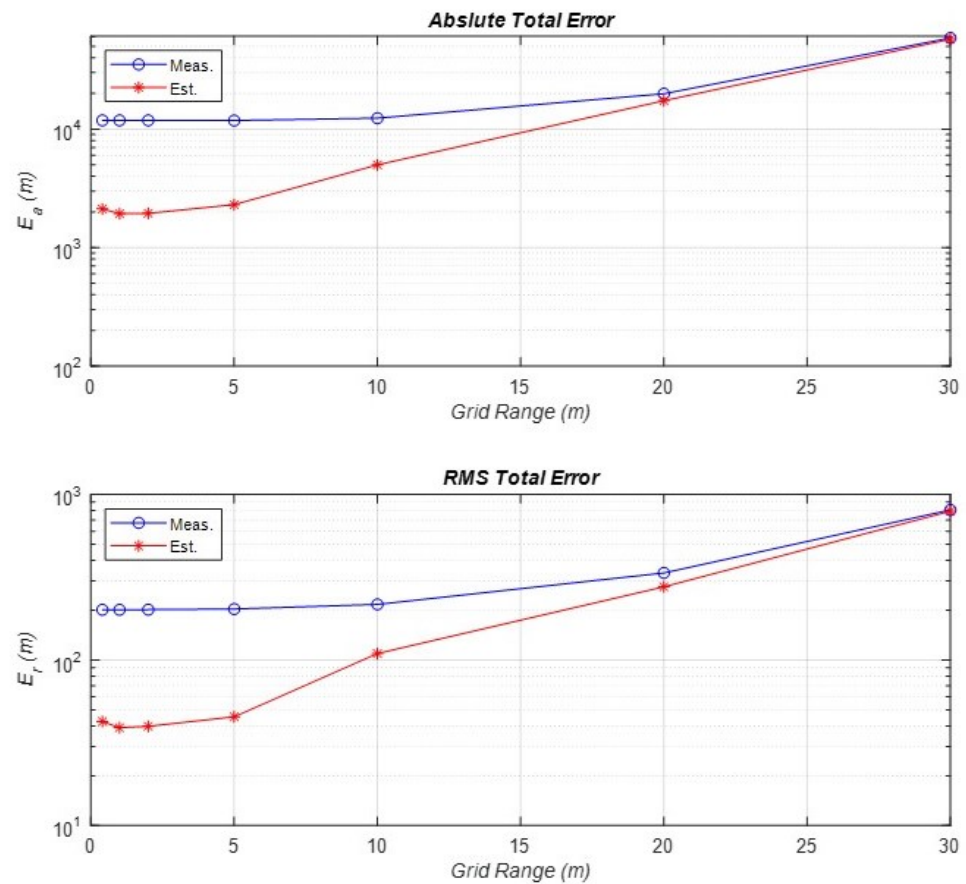


**Figure 9.** Variation in the absolute and RMS total measured errors (blue lines), and the absolute and RMS total estimated errors (red lines) for different grid ranges at a constant beam angle without external disturbances.

#### 4.3. Analysis of the Sonar Position Draft/Bias Effect

The accuracy of the underwater map was analyzed at the positions at which the sonar was away from the sea level, but approaching the seafloor. The slope effect of the seafloor was reduced by placing the acoustic sonar at a known distance from the sea surface,  $h_d$ , as shown in Figure 3 owing to high-resolution measurements obtained near the sea floor.

Figure 10 shows the total absolute and RMS measured error (blue line), and the total absolute and RMS estimated error (red line) at different depths of the echosounder from the sea-surface level at a constant beam angle ( $15^\circ$ ) and grid range (10 m) without external disturbances. If the sonar was on the sea surface,  $h_d = 0$ , the total absolute measured error was  $13 \times 10^3$  m, total absolute estimated error was  $3 \times 10^3$  m, and the total RMS, measured and estimated errors were 200 and 40 m, respectively, at  $g_r = 10$  m,  $\varphi = 15^\circ$ ,  $\delta_x = 0$ ,  $\delta_y = 0$ . When the distance between echosounder and sea surface increased to 5 m, the total absolute measured error was  $10 \times 10^3$  m, total absolute estimated error was  $2 \times 10^3$  m, total RMS measured error was 180 m, and the total RMS estimated error was 30 m at  $g_r = 10$  m,  $\varphi = 15^\circ$ ,  $\delta_x = 0$ ,  $\delta_y = 0$ .

These results show that the absolute measured and estimated errors decreased as the vehicle approached the seafloor. Figure 10 shows that the single-beam echosounder had a higher resolution because the coverage area of the echosounder was narrowing and the vehicle was less affected by external disturbances such as wind and waves when the depth of the echosounder from sea-surface level increased. This result shows that, by considering the grid range in Lemma 2, the requirement of the echosounder was close to the seafloor.

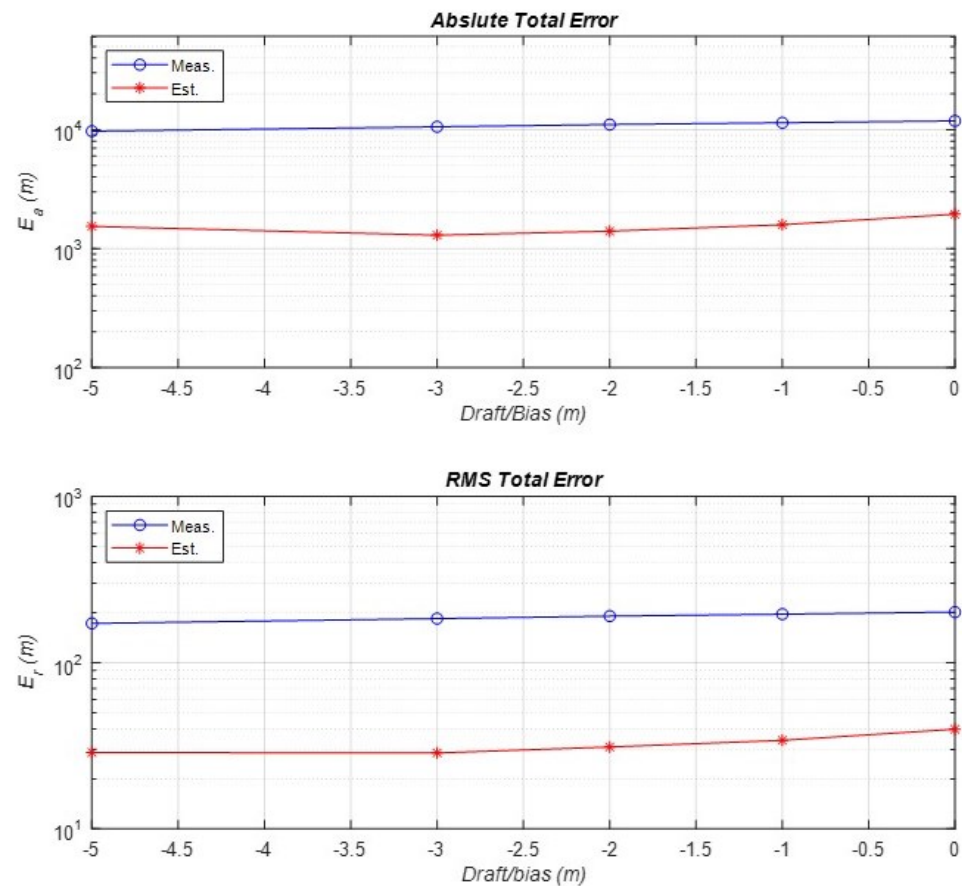


**Figure 10.** Absolute and RMS total measured errors (blue lines), and absolute and RMS total estimated errors (red lines) related to the draft (or bias) of the echosounder from sea-surface level at a constant grid range and beam angle.

#### 4.4. Analysis of the External Disturbances Effect

Changing the position and attitudes of the sea-surface vehicle through external disturbances such as wind and waves affected the measured bathymetric data. The roll and pitch angles of the vehicle were zero without disturbances, and the echosounder was perpendicular to the seafloor. The sea-surface vehicle oscillated in the presence of external disturbances, and the roll and pitch attitudes of the vehicle were different from those of the starting level. Thus, the sea-bottom coverage area changed, and the bathymetric value could not be measured perpendicularly to the seabed, as shown in Figure 3c.

Figure 11 shows the total absolute and RMS measured errors (blue lines), and the total absolute and RMS estimated errors (red lines) at different attitudes of the vehicle integrated with the single-beam echosounder at a constant beam angle ( $15^\circ$ ) and constant grid range (10 m). It was assumed that the depth of the vehicle from the sea-surface was zero in this condition. The disturbance in the x and y axes comprised uniformly distributed random variables with maximal values of  $0^\circ$ ,  $2^\circ$ ,  $4^\circ$  and  $7^\circ$ .

If the rotations of the vehicle with external disturbances in the x and y axes were  $2^\circ$  ( $\delta_x = 2^\circ$ ,  $\delta_y = 2^\circ$ ), the absolute measured error became  $1 \times 10^4$  m, the absolute estimated error was  $3 \times 10^3$  m, RMS measured error was  $2 \times 10^2$  m, and the RMS estimated error was  $9 \times 10^1$  m at  $g_r = 10$ ,  $\varphi = 15^\circ$ ,  $h_d = 0$ . When the external disturbance effect increased to  $7^\circ$  in the x and y axes, the absolute measured error was  $1.5 \times 10^4$  m, the absolute estimated error was  $1 \times 10^4$  m, the RMS measured error was  $2.5 \times 10^2$  m, and the RMS estimated error was  $2 \times 10^2$  m at  $g_r = 10$ ,  $\varphi = 15^\circ$ ,  $h_d = 0$ .

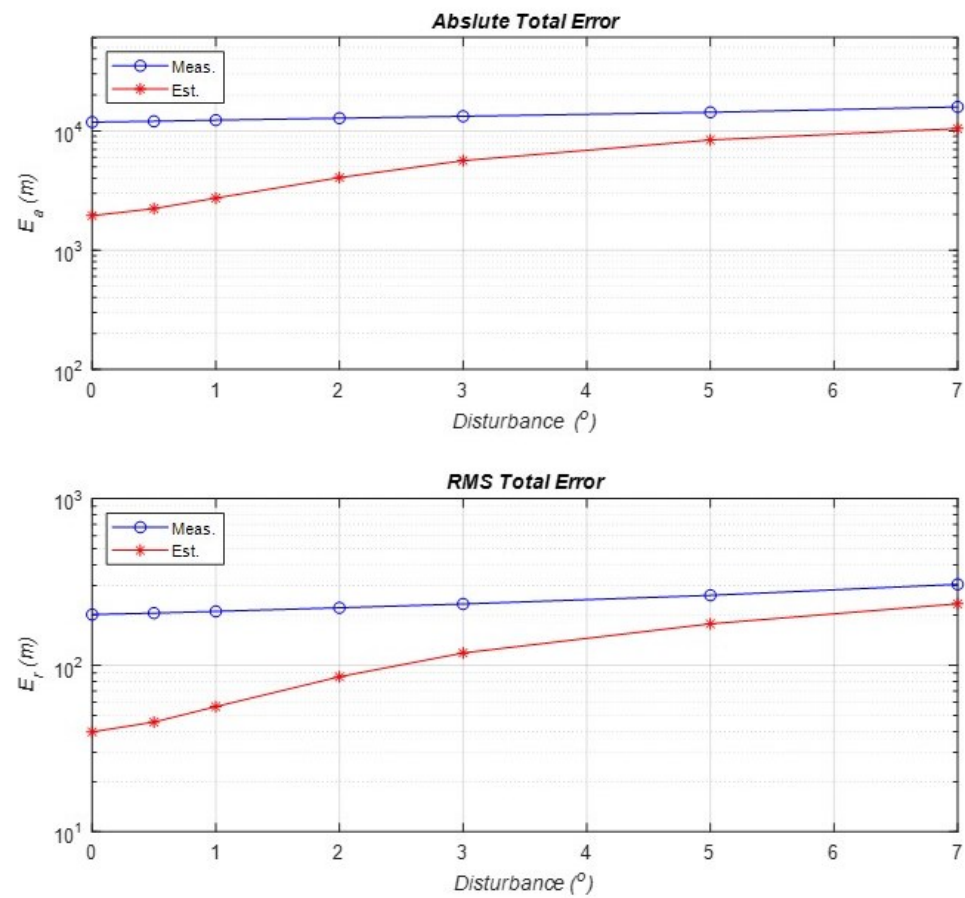


**Figure 11.** Absolute and RMS total measured errors (blue lines), and absolute and RMS total estimated errors (red lines) related to the external-disturbance effect to the oscillation of the sea-surface vehicle at constant grid range and beam angle.

Simulation results show that the absolute measured and estimated errors increased when the external-disturbance effect increased. Thus, it is important to perform measurements when the sea-surface vehicle on which a single-beam echosounder is located is perpendicular to the measuring point in the mapped area.

If the beam angle becomes narrower, without external disturbances, the accuracy of the underwater map increases. However, under external-disturbance conditions, the accuracy is not higher with a narrow beam angle because the measurement of some points may be missed, especially in an inclined sea-bottom area.

### 5. Underwater Mapping Experiment

Experimental bathymetric measurements were performed at the test area, the port of Kozlu in the city of Zonguldak in the Black Sea, Turkey as shown in Figure 12. The date of taking the bathymetric measurements was chosen on the basis of the anticipated wave height. A day with a wave height of at most 0.1 m was deemed to be suitable for this experiment, and it was chosen on the basis of the weather forecast, as shown in Figure 13.

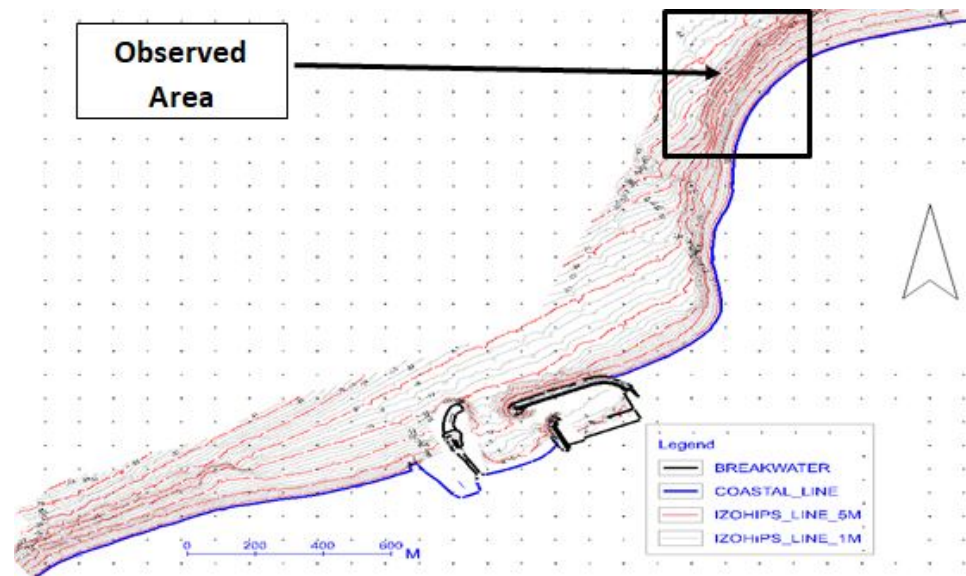


Figure 12. Experimental area from Google Earth view.



Figure 13. Wave prediction map dated 9 September 2020 for the sea-experiment.

Before starting the measurements in the experimental area, the measurement lines were determined in the experimental area as the basis for bathymetric map production. According to the International Hydrographic Organization standards, the maximum line spacing for some coastal areas up to 100 m deep is three times the average depth or 25 m. In this study, it was obtained as 10 m to reveal the bottom topography more clearly. In Figure 14, the transverse and vertical lines are the observation and control lines, respectively. The transverse line spacing was determined as 10 m, and the distance between the control lines was defined as approximately 20 m. The all-test area was mapped in one day. The tide value at the time of the bathymetry study was added to the measured values. One of the critical sources of error in the acoustic sounding method is the incorrect measurement of the speed of sound. The speed of sound assumes different values in different environments, such as lakes, salt water, and fresh water. The sound velocity was measured at different depths in the experimental area to obtain a more accurate map. An AML Minos-X brand CSTD device used for sound velocity measurement is shown in Figure 15. The sound velocity was measured as 1469 m/s, and then used for data analysis. The properties of the single-beam echosounder used to measure the depths in this study are listed in Table 1; we used 120 kHz.



**Figure 14.** Bathymetric survey plan for the sea-experiment area.

Figure 15 shows the sea-surface vehicle integrated with measurement devices used in the experiment. Bathymetric data were measured using the single-beam echosounder located on the sea-surface vehicle. Navigation data were measured using global positioning system (GPS) devices. A compatible global navigation satellite system (GNSS) receiver with the Continuously Operating Reference Station-Turkey (CORS-TR) network was used for the purpose of providing the navigation of the unmanned surface vehicle. The national Continuously Operating Reference Station (CORS) networks, which operate on the real-time kinematic (RTK) principle, are multipurpose geodetic networks. Using this method, the horizontal position of the GNSS receiver could be determined with a horizontal sensitivity of  $\pm 1\text{--}2$  cm.

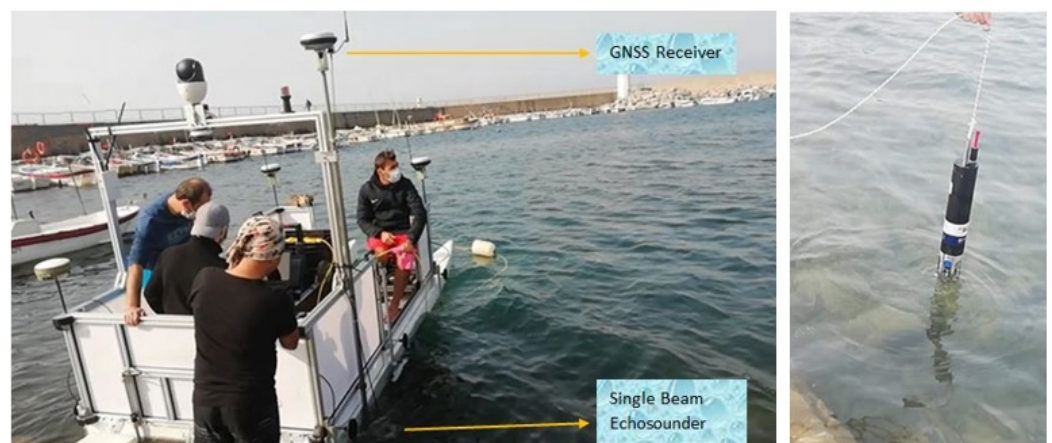


**Figure 15.** Sea-surface vehicle integrated with measurement devices used in the experiment, and the measurement of the acoustic sound velocity in the sea before the experiment (right side).

Raw measurement data were used to create a depth model of the project area. The linear interpolation method was preferred for this depth model. The isobath map of the region was created using the depth model as shown in Figure 14. To investigate the errors caused by the slope of the bottom topography, a region where the depth changes was chosen in the observed area. This region is illustrated in Figure 14. The errors caused by the slope of the topography were modeled, and a second map of the same region was created. Furthermore, the differences between them were analyzed in a MATLAB, HYPACK, and Global Mapper environment.

**Table 1.** Properties of the single-beam echosounder used in this study.

Frequency	24 kHz–210 kHz
Depth	5–5000 m
Acoustic velocity	1300–1800 m/s
Accuracy	at—0–100 m, 1 cm
Beam spread	±4 minimal degrees

The sea-bottom slope angles in the  $x$  and  $y$  axes were calculated on the basis of (5) and (6) using the measured bathymetric data in the experimental area. Figure 16 shows the estimated sea-bottom slope angles in the  $x$  axis represented by  $\alpha$ , and the  $y$  axis represented by  $\beta$  for the observed experimental area, where the depths changed suddenly.

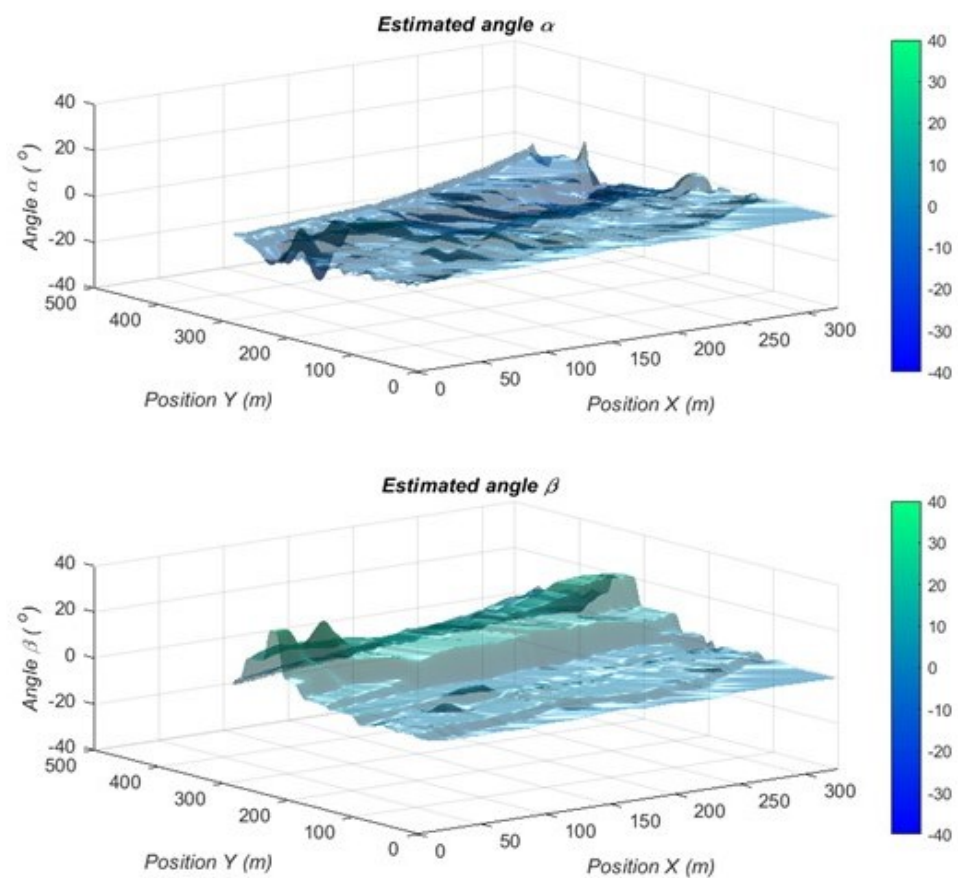


**Figure 16.** Estimated sea-bottom slope angles in the  $x$  ( $\alpha$ ) and  $y$  ( $\beta$ ) axes in the experimental area based on experimental data.

Subsequently, the measured bathymetric data were corrected in relation to the estimated bottom slope angles. Figure 17 shows the underwater maps with measured and corrected depth levels.

Figure 18 shows the depth difference between the corrected and measured maps. Figure 18 shows that there were depth differences of up to 5 m between the measured and the corrected map. This shows that the measured bathymetric data should have been corrected on the basis of seafloor slope angles. The underwater map obtained without considering the seafloor slope, and one with correction based on the bottom slope angles were compared. Figure 19 shows the model differences on the basis of the slope of the bottom topography. The bottom side of Figure 19 shows the corrected map, and the

upper side of Figure 19 shows the underwater map without correction. Figure 19 shows that the measured underwater topography without considering the bottom slope angles appeared to be an inclined area. Thus, a more accurate underwater map was obtained with this correction.

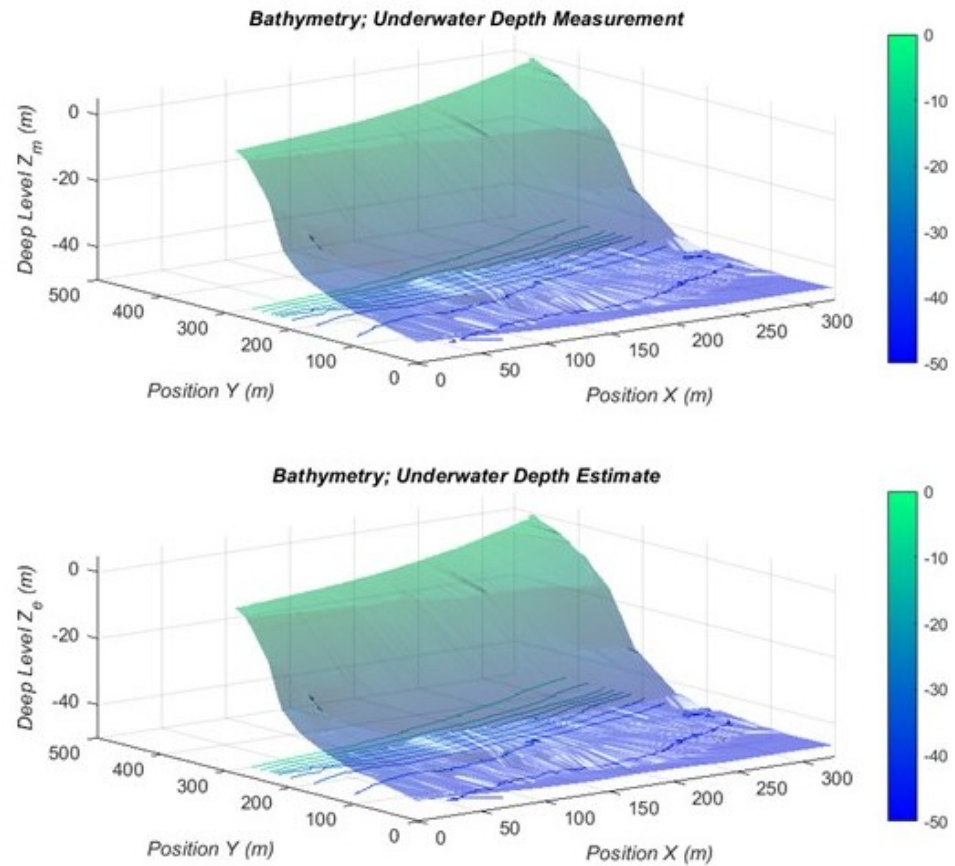


Figure 17. Underwater map with (top) measured and (bottom) estimated depth levels based on experimental data.

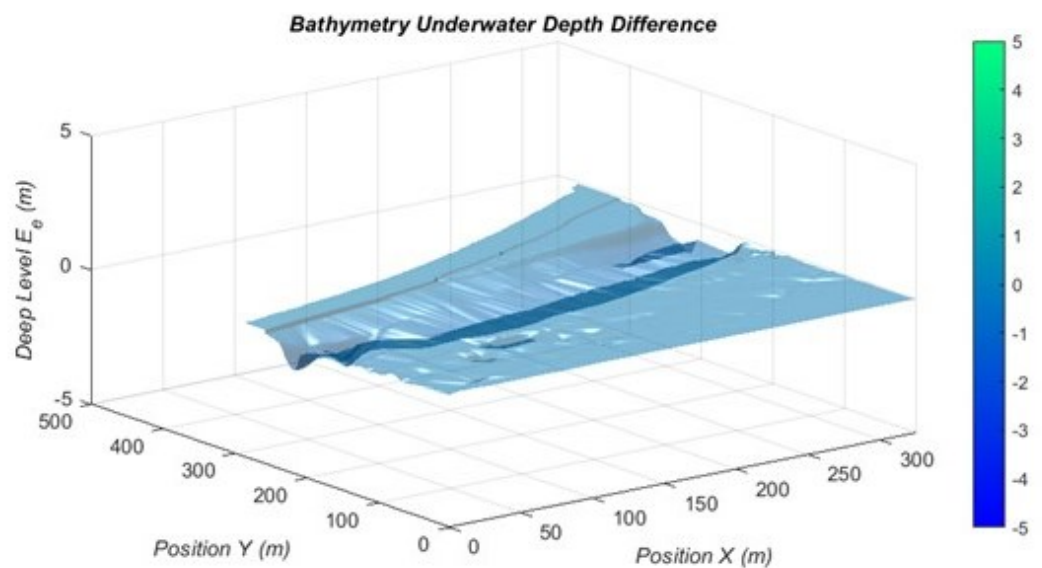


Figure 18. Underwater depth differences between the corrected and measured maps.

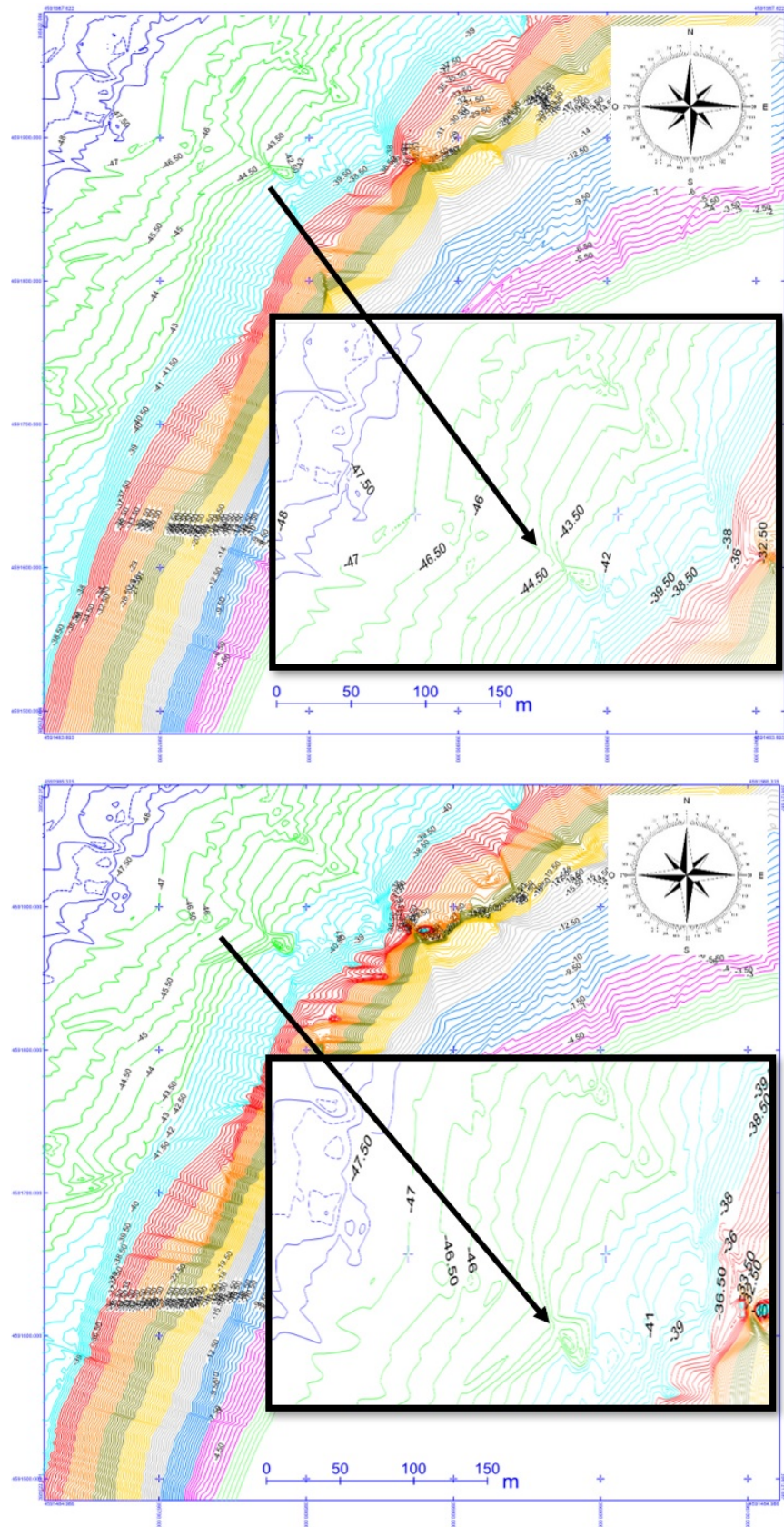


Figure 19. (top) Bottom topography model based on the measured map. (bottom) Corrected map model based on the slope of the bottom topography.

## 6. Conclusions

In this study, an underwater map was modeled and analyzed on the basis of a simulation. Experimental data were obtained from a single-beam echosounder by navigating a sea-surface vehicle. Factors that influence underwater mapping accuracy, namely, seafloor slope angle, the grid range of the mapped area, the beam angle of the echosounder, the position of the echosounder, and the oscillation of sea-surface vehicles owing to external disturbances were analyzed. The underwater mapping created experimentally for the Kozlu/Zonguldak area was corrected by estimating the sea-bottom slope angle and using it to correct the bathymetric data. As indicated by the simulation results, the accuracy of the underwater map was higher when the beam angle was narrower, and the grid range shrank without external disturbances. The error in the measurements owing to the oscillation of the vehicle increased with the external disturbances. The results indicate that more accurate underwater mapping is obtained depending on the received bathymetric data when the sea-surface vehicle on which the echosounder is integrated nears the seafloor. This is because when the vehicle in which the echosounder is integrated approaches the seafloor, external disturbances such as wind and waves cannot affect the movement of the vehicle; thus, the error in the measured bathymetric data is decreased. In addition, higher resolution data are obtained by the vehicle when it is close to the seafloor, and in some areas that the surface vehicle cannot reach, an underwater map can still be completed. All these results indicate that the underwater map created with bathymetric data, obtained by integrating the echosounder into the underwater vehicle rather than a sea-surface vehicle, is more accurate. In future studies, we will compare the results of an experiment performed in the same test area with the bathymetric data obtained using an unmanned underwater vehicle [41].

**Author Contributions:** Data curation, S.K.K. and R.H.; Formal analysis, S.K.K., R.H., K.S.G. and Ş.H.K.; Investigation, S.K.K. and K.S.G.; Methodology, S.K.K., R.H., Ş.H.K. and M.K.L.; Resources, K.S.G. and Ş.H.K.; Software, R.H.; Visualization, S.K.K. and R.H.; Writing—original draft, S.K.K.; Writing—review & editing, R.H., K.S.G., Ş.H.K. and M.K.L. All authors have read and agreed to the published version of the manuscript.

**Funding:** This work is supported by the Scientific and Technological Research Council of Turkey (grant 119E037).

**Institutional Review Board Statement:** Not applicable.

**Informed Consent Statement:** Not applicable.

**Data Availability Statement:** Not applicable.

**Acknowledgments:** This work is supported by the Scientific and Technological Research Council of Turkey (grant 119E037). The authors are grateful for the support of the Scientific and Technological Research Council of Turkey.

**Conflicts of Interest:** The authors declare no conflict of interest.

## References

1. Guan, M.; Cheng, Y.; Li, Q.; Wang, C.; Fang, X.; Yu, J. An Effective Method for Submarine Buried Pipeline Detection via Multi-Sensor Data Fusion. *IEEE Access* **2019**, *7*, 125300–125309. [[CrossRef](#)]
2. Florinsky, I.V.; Filippov, S.V. Three-Dimensional Geomorphometric Modeling of the Arctic Ocean Submarine Topography: A Low-Resolution Desktop Application. *IEEE J. Ocean. Eng.* **2021**, *46*, 88–101. [[CrossRef](#)]
3. Bosch, J.; Istenic, K.; Gracias, N.; Garcia, R.; Ridaio, P. Omnidirectional Multicamera Video Stitching Using Depth Maps. *IEEE J. Ocean. Eng.* **2020**, *45*, 1337–1352. [[CrossRef](#)]
4. Yin, J.; Wang, Y.; Lv, J.; Ma, J. Study on Underwater Simultaneous Localization and Mapping Based on Different Sensors. In Proceedings of the IEEE 10th Data Driven Control Learning Systems Conference, Suzhou, China, 14–16 May 2021; pp. 728–733. [[CrossRef](#)]
5. Ni, H.; Wang, W.; Ren, Q.; Lu, L.; Wu, J.; Ma, L. Comparison of Single-beam and Multibeam Sonar Systems for Sediment Characterization: Results from Shallow Water Experiment. In Proceedings of the IEEE Oceans MTS/IEEE Seattle, Seattle, WA, USA, 27–31 October 2019; pp. 1–4. [[CrossRef](#)]

6. Zhao, J.; Yan, J.; Zhang, H.; Zhang, Y.; Wang, A. A new method for weakening the combined effect of residual errors on multibeam bathymetric data. *Mar. Geophys. Res.* **2014**, *35*, 379–394. [[CrossRef](#)]
7. I. H. Organization, Manual on Hydrography. International Hydrographic Bureau Publication. 2005. Available online: [https://www.deparentis.com/wp-content/uploads/2020/04/IHO-Manual-on-Hydrography-1st-edition-February-2011-C-13\\_e1.0.0\\_ENG.pdf](https://www.deparentis.com/wp-content/uploads/2020/04/IHO-Manual-on-Hydrography-1st-edition-February-2011-C-13_e1.0.0_ENG.pdf) (accessed on 3 June 2022).
8. Foote, K. Using a sonar in a different environment from that of its calibration: Effects of changes in salinity and temperature. In Proceedings of the IEEE OCEANS, Charleston, SC, USA, 22–25 October 2018; pp. 1–5. [[CrossRef](#)]
9. Lurton, X. Swath Bathymetry Using Phase Difference: Theoretical Analysis of Acoustical Measurement Precision. *IEEE J. Ocean. Eng.* **2000**, *25*, 351–363. [[CrossRef](#)]
10. Malik, M. Sources and Impacts of Bottom Slope Uncertainty on Estimation of Seafloor Backscatter from Swath Sonars. *Geosciences* **2019**, *9*, 183. [[CrossRef](#)]
11. N, A.; Gavrilov.; Parnum, I.M. Fluctuations of Seafloor Backscatter Data From Multibeam Sonar Systems. *IEEE J. Ocean. Eng.* **2010**, *35*, 209–219. [[CrossRef](#)]
12. Biffard, B.R.; Preston, J.M.; Chapman, N.R. Acoustic Classification with Single-Beam Echosounders: Processing Methods and Theory for Isolating Effects of the Seabed on Echoes. In Proceedings of the IEEE OCEANS, Vancouver, BC, Canada, 29 September–4 October 2007; pp. 1–8. [[CrossRef](#)]
13. Biffard, B.; Bloomer, S.; Chapman, N. The Role of Echo Duration in Acoustic Seabed Classification and Characterization. In Proceedings of the Oceans MTS/IEEE Seattle, Seattle, WA, USA, 20–23 September 2010; pp. 1–8.
14. Garcia, D.C.; de Queiroz, R.L.; Rocha, M.P.; da Fonseca, L.E. Automatic compensation for seafloor slope and depth in post-processing recovery of seismic amplitudes. In Proceedings of the IEEE/OES Acoustics in Underwater Geosciences Symposium (RIO Acoustics), Rio de Janeiro, Brazil, 25–27 July 2017; pp. 1–5.
15. Song, G.S.; Lo, S.C.; Fish, J.P. Underwater Slope Measurement Using a Tilted Multibeam Sonar Head. *IEEE J. Ocean. Eng.* **2014**, *39*, 419–429. [[CrossRef](#)]
16. Bird, J.S.; Mullins, G.K. Analysis of Swath Bathymetry Sonar Accuracy. *IEEE J. Ocean. Eng.* **2005**, *30*, 372–390. [[CrossRef](#)]
17. Sangekar, M.N.; Thornton, B.; Bodenmann, A.; Ura, T. Autonomous Landing of Underwater Vehicles Using High-Resolution Bathymetry. *IEEE J. Ocean. Eng.* **2019**, *5*, 1252–1267. [[CrossRef](#)]
18. Fujiwara, T.; and Fujio Yamamoto, Y.M. Evaluation of spatial resolution and estimation error of seafloor displacement observation from vessel-based bathymetric survey by use of AUV-based bathymetric data. *Mar. Geophys. Res.* **2015**, *36*, 45–60. [[CrossRef](#)]
19. Becker, J.J.; Sandwell, D.T. Global estimates of seafloor slope from single-beam ship soundings. *J. Geophys. Res.* **2008**, *113*. [[CrossRef](#)]
20. EL-Hattab, A.I. Single beam bathymetric data modelling techniques for accurate maintenance dredging. *Egypt. J. Remote Sens. Space Sci.* **2014**, *17*, 189–195. [[CrossRef](#)]
21. Daniell, J.J. Development of a bathymetric grid for the Gulf of Papua and adjacent areas: A note describing its development. *J. Geophys. Res.* **2008**, *113*. [[CrossRef](#)]
22. Beyer, A.; Schenke, H.; Klenke, M.; Niederjasper, F. High resolution bathymetry of the eastern slope of the Porcupine Seabight. *Elsevier Mar. Geol.* **2003**, *198*, 27–54. [[CrossRef](#)]
23. Martin Jakobsson, B.C.; Mayer, L. On the effect of random errors in gridded bathymetric compilations. *J. Geophys. Res.* **2002**, *107*, 2358. [[CrossRef](#)]
24. Mirjam Snellen, K.S.; Simons, D.G. Model-based sediment classification using single-beam echosounder signals. *J. Acoust. Soc. Am.* **2011**, *129*, 2878–2888. [[CrossRef](#)]
25. Christou, C.T.; Jacyna, G.M. Simulation of the Beam Response of Distributed Signals. *IEEE Trans. Signal Process.* **2005**, *53*, 3023–3031. [[CrossRef](#)]
26. Kuperman, W.; Roux, P. Underwater Acoustics. In *Springer Handbook of Acoustics*; Rossing, T., Ed.; Springer: New York, NY, USA, 2007; pp. 149–204. [[CrossRef](#)]
27. Doisy, Y. Theoretical Accuracy of Doppler Navigation Sonars and Acoustic Doppler Current Profilers. *IEEE J. Ocean Eng.* **2004**, *29*, 430–441. [[CrossRef](#)]
28. Bishop, G.C. Gravitational field maps and navigational errors. In Proceedings of the 2000 International Symposium on Underwater Technology (Cat. No.00EX418), Tokyo, Japan, 26 May 2000; pp. 149–154. [[CrossRef](#)]
29. Edward Chen, J. Realtime map generation using side scan sonar scanlines for unmanned underwater vehicles. *Ocean Eng.* **2014**, *91*, 252–262. [[CrossRef](#)]
30. Guo, Y. 3D Underwater Topography Rebuilding Based on Single Beam Sonar. In Proceedings of the IEEE International Conference on Signal Processing, Communication and Computing, KunMing, China, 5–8 August 2013; pp. 1–5. [[CrossRef](#)]
31. Sac, H.; Leblebicioglu, K.; Akar, G.B. 2D high-frequency forward-looking sonar simulator based on continuous surfaces approach. *Turk. J. Electr. Eng. Comput. Sci.* **2015**, *23*, 2289–2303. [[CrossRef](#)]
32. Gürtürk, F.F. Error Analysis of Seabed Mapping Using Multibeam Sonar. Master’s Thesis, Middle East Technical University, Ankara, Turkey, 2015.
33. Pailhas, Y.; Brown, K.; Capus, C.; Petillot, Y. Design of artificial landmarks for underwater simultaneous localisation and mapping. *IET Radar Sonar Navig.* **2013**, *7*, 10–18. [[CrossRef](#)]

34. Ma, X.; Yanli, C.; Bai, G.; Liu, J. Multi-AUV Collaborative Operation Based on Time-Varying Navigation Map and Dynamic Grid Model. *IEEE Access* **2020**, *8*, 159424–159439. [[CrossRef](#)]
35. Casas, S.B.F. *A Concise Introduction to Geometric Numerical Integration*; CRC Press, Taylor & Francis Group: Boca Raton, FL, USA, 2017.
36. Kendall, E.A.; Weimin Han, D.S. *Numerical Solution of Ordinary Differential Equations*; A John Wiley & Sons, INC. Publication: Hoboken, NJ, USA, 2009.
37. Karadeniz Kartal, S.; Leblebicioglu, M.K.; Ege, E. Experimental test of the acoustic-based navigation and system identification of an unmanned underwater survey vehicle (SAGA). *Trans. Inst. Meas. Control* **2018**, *40*, 2476–2487. [[CrossRef](#)]
38. Karadeniz Kartal, S.; Casalino, G. Horizontal Parking Control of Autonomous Underwater Vehicle, FOLOGA. *IFAC-PapersOnLine* **2019**, *52*, 397–402. [[CrossRef](#)]
39. El-Diasty, M. Development of Real-Time PPP-Based GPS/INS Integration System Using IGS Real-Time Service for Hydrographic Surveys. *J. Surv. Eng.* **2016**, *142*, 05015005. [[CrossRef](#)]
40. Belge, E.; Cantekin, R.; Erol, B.; Akgul, V.; Kartal, S.K.; Hacioglu, R.; Gormus, S.; Kutoglu, H.; Leblebicioglu, K. Sensor Fusion Based on Integrated Navigation Data of Sea Surface Vehicle with Machine Learning Method. In Proceedings of the IEEE International Conference on Innovations in Intelligent Systems and Applications, Kocaeli, Turkey, 25–27 August 2021; pp.1–6. [[CrossRef](#)]
41. Erol, B.; Cantekin, R.; Kartal, S.K.; Hacioglu, R.; Gormus, S.; Kutoglu, H.; Leblebicioglu, K. Estimation of Unmanned Underwater Vehicle Motion with Kalman Filter and Improvement by Machine Learning. *Int. J. Adv. Eng. Pure Sci.* **2021**, *33*, 67–77.